Journal of Zhejiang University SCIENCE A
ISSN 1009-3095
http://www.zju.edu.cn/jzus
E-mail: jzus@zju.edu.cn

Review:

Broad-bandwidth and low-loss metamaterials: theory, design and realization

LI Le-wei (李乐伟)[†1,2], YAO Hai-ying (姚海英)[1], WU Qun (吴 群)[2], CHEN Zhi-ning (陈志宁)[1,3]

([1]*Department of Electrical and Computer Engineering, The National University of Singapore, 119260, Singapore*)

([2]*Department of Electronics and Communications Engineering, Harbin Institute of Technology, Harbin 150001, China*)

([3]*Institute for Infocomm Research, 117674, Singapore*)

[†]E-mail: LWLi@nus.edu.sg

Received Sept. 5, 2005; revision accepted Oct. 10, 2005

Abstract: In this paper, we summarize some recent activities in the field of metamaterial research at the National University of Singapore (NUS). Integral equations are applied for electromagnetic modelling of supernatural materials. Some special characteristics of the metamaterials are shown. Moreover, quasi-static Lorentz theory and numerical method (i.e., the method of moments for solving the electric field integral equation) and the transmission line theory are both presented to obtain the effective constitutive relations of metamaterials, respectively. Finally, feasibility of fabricating metamaterials based on analysis of equivalent transmission line model in the microwave spectrum and even higher is also shown and correspondingly some broad-bandwidth and low-loss metamaterial structures are designed and synthesized.

Key words: Metamaterials, Electric field integral equation (EFIE), Transmission line theory (TLT), Quasi-static Lorentz theory
doi:10.1631/jzus.2006.A0005 **Document code:** A **CLC number:** O441

INTRODUCTION

Conventional materials have positive magnetic permeability and mostly positive electrical permittivity. Veselago (1968) initially assumed a material with negative permittivity and permeability simultaneously and theoretically demonstrated the abnormal electromagnetic properties. This material, referred to as left-handed material (LHM) or metamaterial, reverses a basic feature of light, such as, the reversal of the Doppler shift for radiation, and negative refractive index (NRI). However, research work in this area did not draw much attention in the engineering and physics communities until Pendry *et al*.(1996; 1999) and Pendry (2000) theoretically formulated the LHM, in particular, a concept of perfect lens was brought forward although only superlens is accepted by the community later on. Smith *et al*.(2000) further studied the LHM, and experimentally realized this material with periodically-arranged conducting concrete. The artificial material is very different from the natural material, and shows extraordinary properties. It was later referred to as metamaterials.

Properties of negative permittivity and permeability of artificial metamaterials can be realized from different physical or mechanical synthesis and fabrication methodologies. Although general periodic structures can be fabricated to yield the special properties, the primary material synthesis is still made based on the individual inclusions (Falcone *et al.*, 2004; Smith and Schurig, 2003; Ziolkowski, 2003; Engheta, 2003; Gay-Balmaz and Martin, 2001; Li *et al*., 2003) or the L-C microwave striplines/devices (Caloz *et al.*, 2004; Oliner, 2003; Grbic and Eleftheriades, 2003). To design such artificial materials for different specific engineering applications, simulation tools are essential for saving efforts and costs. The numerical methods for characterizing these structures are still those fundamental numerical simulation techniques, that is, the differential equation (DE)

method (Chen *et al.*, 2003; Weiland *et al.*, 2001), the integral equation (IE) method (Gay-Balmaz and Martin, 2002; Yao *et al.*, 2004; 2005), and the equivalent circuit models (Sanada *et al.*, 2004; Xu *et al.*, 2004a; 2004b; Eleftheriades *et al.*, 2002).

In this review paper, we present some recent results of our investigations into the metamaterials. The propagation properties of a beamed plane electromagnetic wave into the metamaterial prism are presented firstly. Especially, we show the existence of the negative refraction phenomenon. In this process, the electromagnetic solution developed based on the method of moments (MoM) for solving the electric field integral equation (EFIE) is applied. A fast algorithm is further developed based on the modified Gram-Schmidt (MGS) procedure and integrated into the MoM procedure to accelerate the matrix-vector multiplications. It can reduce both the computational complexity and the memory requirement (Yao *et al.*, 2005). The effective constitutive parameters of the metamaterials are finally estimated utilizing the quasi-static Lorentz theory and numerical method (Yao *et al.*, 2004) and transmission line theory (TLT) (Xu *et al.*, 2005a; 2005b). Use of the TLT yielded the design techniques to obtain a wide bandwidth and low-loss metamaterial. Here we configure some new periodic structures, which are synthesized based on the microstrip lines/devices, split ring resonators (SRRs) and rods. Some special optical phenomena, such as negative refraction and image effect, are presented to show the availability of these structures (Xu *et al.*, 2004a; 2004b; 2005a; 2005b).

ELECTROMAGNETIC MODELLING OF METAMATERIALS

Surface integral equation

The inclusions to construct the metamaterials are usually made of conductors. In this paper, we consider them as perfect ones. For a perfectly electricity conducting (PEC) object illuminated by a plane wave $\boldsymbol{E}^{\mathrm{i}}$, the EFIE can be obtained by enforcing the boundary conditions of the tangential electric field components on its surface, and is given by

$$\hat{\boldsymbol{t}}\cdot\int_s\left(J(\boldsymbol{r}')+\frac{1}{\boldsymbol{k}^2}\nabla'\cdot J(\boldsymbol{r}')\nabla\right)g(\boldsymbol{r},\boldsymbol{r}')\mathrm{d}s'=-\frac{4\pi\mathrm{j}}{\boldsymbol{k}\eta_0}\hat{\boldsymbol{t}}\cdot\boldsymbol{E}^{\mathrm{i}}(\boldsymbol{r}) \tag{1}$$

where J is the induced current density, $\hat{\boldsymbol{t}}$ denotes the unit tangential vectors of the surface s, η_0 and $\boldsymbol{k}$ stand for the wave impedance and the propagation constant in free space respectively, and

$$g(\boldsymbol{r},\boldsymbol{r}')=\mathrm{e}^{-\mathrm{j}\boldsymbol{k}_0|\boldsymbol{r}-\boldsymbol{r}'|}\Big/|\boldsymbol{r}-\boldsymbol{r}'|.$$

The standard MoM technique is used to solve the equation subsequently. After discretizing the unknown currents, an algebraic matrix equation is taken as inner products with proper testing functions, which is formulated by

$$\bar{\boldsymbol{A}}\boldsymbol{a}=\boldsymbol{b}, \tag{2}$$

where $\bar{\boldsymbol{A}}$ denotes an impedance matrix, and $\boldsymbol{a}$ identifies an unknown column vector while $\boldsymbol{b}$ represents a coefficient column vector.

Evidently, the impedance matrix $\boldsymbol{A}$ requires a storage of $O(N^2)$. A direct solver for Eq.(2) requires $O(N^3)$ computational cost and an iterative solver requires $O(N^2)$ per iteration. Once the number N of unknowns becomes large, these requirements could easily run out of the given memory and the efficiency will become very poor. To resolve this problem, an algorithm based on the modified Gram-Schmidt procedure is applied (Yao *et al.*, 2005), which can reduce both the computational complexity and the memory requirement to $O(N^{1.5})$. First, we divide the basis functions into groups. For every group, a local MoM matrix must be calculated. Then, utilizing these column vectors in the local matrix, the modified Gram-Schmidt orthogonalization procedure is performed to decompose this matrix. Thus, two matrices obtained by this operation are used in the iterative solver to replace the local matrices.

Numerical results

In this section, a metamaterial prism (as a wedge-shaped sample) synthesized by the inclusions shown in Fig.1 is considered and depicted in Fig.2.

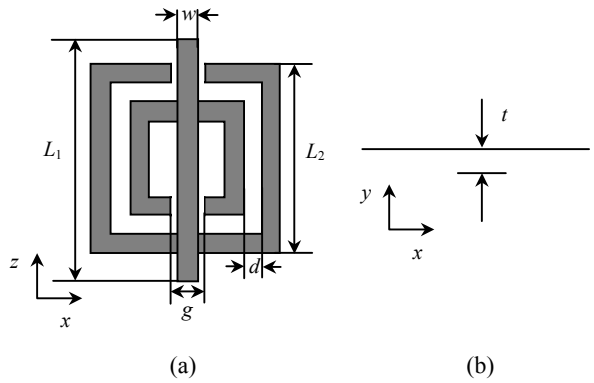

(a) (b)

Fig.1 Geometry of a single inclusion composed by a square SRR and a wire. The dimensions are assumed to be L_1=3.3 mm, L_2=2.63 mm, w=0.25 mm, d=0.3 mm, g=0.46 mm, and t=0.254 mm. (a) Front view; (b) Top view

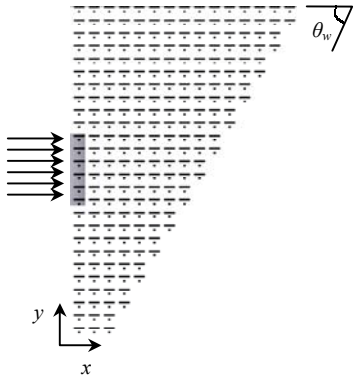

Fig.2 Top view of a metamaterial prism

The space distances of the inclusions, denoted respectively by d_x, d_y, and d_z in the x-, y- and z-directions, are all 3.3 mm. The total number of inclusions is 234. The numbers of inclusions along the shortest side and the longest side are 3 and 15, respectively. The incline angle θ_w of this prism is about 63.43°. In this case, the incident angle θ^{i} is 25.64°. The MGSA needs 119.5 MB of memory and takes 0.13 s per iteration.

First, the scattering cross section (SCS) of a single inclusion is evaluated to find the resonant frequency, which is shown in Fig.3. It can be found that the resonant frequency is about 16.25 GHz. Subsequently, we employ the MGS algorithm to analyze the propagation characteristics of electromagnetic wave in the metamaterial sample, which is placed in free space. In order to gain more insight into the effects or influences of the prism edge of the metamaterials, we consider a beamed plane wave as the incidence, which is displayed as the shadow part in Fig.2 and it thus illuminates normally on the first interface. Due to the existence of a small passband near the resonant frequency of the inclusion (Moss, 2002), we calculate the field distribution in a frequency range at f=15.2~17.0 GHz with a step of 0.1 GHz. Fig.4 depicts the amplitude of the electric field component $E_z(\boldsymbol{r})$ versus the frequency, in which E_z is obtained at a 100λ distance of the prism. We can observe a special phenomena around 16.2 GHz. At this frequency, the electric field refracted by the metamaterial wedge peaks at a negative refractive angle. To obtain more details, we also evaluate the field distribution in the frequency range of f=16.1~16.3 GHz with a step of 0.01 GHz. The negative refraction occurred around f=16.21 GHz, which is near the resonance of the inclusion. In Fig.5, we plot the amplitude of electric field component $E_z(\boldsymbol{r})$ at f=16.21 GHz. From this figure, the refractive angle θ_n is found to be about −5.36° and the corresponding refractive index n is −0.2159. The time-harmonic field $E_z(\boldsymbol{r}, t)$ at 16.21 GHz is shown in Fig.6, in which the phase angle is ωt=100°.

EXTRACTION OF CONSTITUTIVE RELATIONS TENSOR PARAMETERS

Quasi-static Lorentz theory with numerical method

A general form of bianisotropic constitutive relations can be expressed in terms of D and B as a function of $\boldsymbol{E}$ and $\boldsymbol{H}$ (Kong, 2002) as follows:

$$\begin{bmatrix} D \\ B \end{bmatrix} = \begin{bmatrix} \bar{\varepsilon} & \bar{\xi} \\ \bar{\varsigma} & \bar{\mu} \end{bmatrix} \begin{bmatrix} \boldsymbol{E} \\ \boldsymbol{H} \end{bmatrix} \tag{3}$$

where $\bar{\varepsilon}$ and $\bar{\mu}$ represent the electric permittivity and magnetic permeability tensors, while $\bar{\xi}$ and $\bar{\varsigma}$ denote the magnetoelectric cross coupling tensors, respectively.

After taking into account electrically small inclusions, our deductions begin with the electric and magnetic dipole moments ($\boldsymbol{p}_{\mathrm{e}}$, $\boldsymbol{p}_{\mathrm{m}}$) based on the quasi-static Lorentz theory (Collin, 1991). A conducting inclusion with arbitrary shape can be characterized by the generalized electromagnetic po-

larizability matrix $[\bar{\alpha}]$, defining the relations between the incident electric and magnetic fields $\boldsymbol{E}^{\mathrm{i}}$ and $\boldsymbol{H}^{\mathrm{i}}$. The induced electric and magnetic dipole moments relate to the incident electric and magnetic fields as follows:

$$\begin{bmatrix} \boldsymbol{p}_{\mathrm{e}} \\ \boldsymbol{p}_{\mathrm{m}} \end{bmatrix} = \begin{bmatrix} \bar{\alpha}_{\mathrm{ee}} & \bar{\alpha}_{\mathrm{em}} \\ \bar{\alpha}_{\mathrm{me}} & \bar{\alpha}_{\mathrm{mm}} \end{bmatrix} \begin{bmatrix} \boldsymbol{E}^{\mathrm{i}} \\ \boldsymbol{H}^{\mathrm{i}} \end{bmatrix} = [\bar{\alpha}] \begin{bmatrix} \boldsymbol{E}^{\mathrm{i}} \\ \boldsymbol{H}^{\mathrm{i}} \end{bmatrix} \tag{4}$$

where

$$\boldsymbol{p}_{\mathrm{e}} = \int_S \rho_{\mathrm{e}}(\boldsymbol{r})\boldsymbol{r}\mathrm{d}s = \frac{\mathrm{j}}{\omega}\int_S \nabla \cdot J_{\mathrm{e}}(\boldsymbol{r})\boldsymbol{r}\mathrm{d}s \tag{5a}$$

$$\boldsymbol{p}_{\mathrm{m}} = \frac{\mu_0}{2}\int_S \boldsymbol{r} \times J_{\mathrm{e}}(\boldsymbol{r})\mathrm{d}s \tag{5b}$$

with the electric current J_{e} on the surface of a conducting inclusion induced by the incident fields.

Using the polarizability matrix $[\bar{\alpha}]$, a general expression for the constitutive relations of metamaterials given by Ishimaru *et al*.(2003) can be rewritten as

$$\begin{bmatrix} \bar{\varepsilon} & \bar{\xi} \\ \bar{\varsigma} & \bar{\mu} \end{bmatrix} = \begin{bmatrix} \varepsilon_0\varepsilon_{\mathrm{h}}\boldsymbol{U} & 0 \\ 0 & \mu_0\boldsymbol{U} \end{bmatrix} + \frac{1}{\Delta V}[\bar{\alpha}]\left[\bar{\boldsymbol{U}} - \frac{1}{\Delta V}\bar{\boldsymbol{C}}[\bar{\alpha}]\right]^{-1} \tag{6}$$

where ε_{h} is the relative dielectric constant of the host materials, $\boldsymbol{U}$ is unit matrix, while the elementary volume ΔV, the coupling matrix $\bar{\boldsymbol{C}}$, and the interaction constant matrix $\boldsymbol{C}$ are defined as

$$\Delta V = d_x d_y d_z, \tag{7a}$$

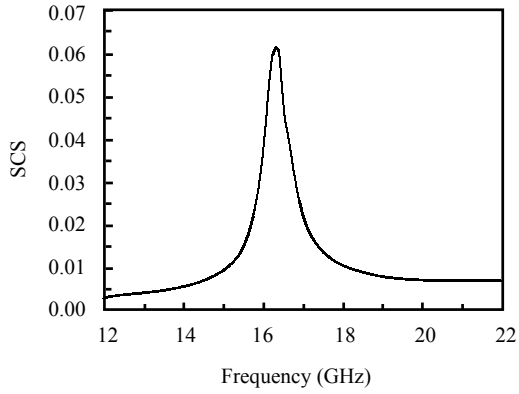

Fig.3 Scattering cross section (SCS) versus frequency for a single inclusion

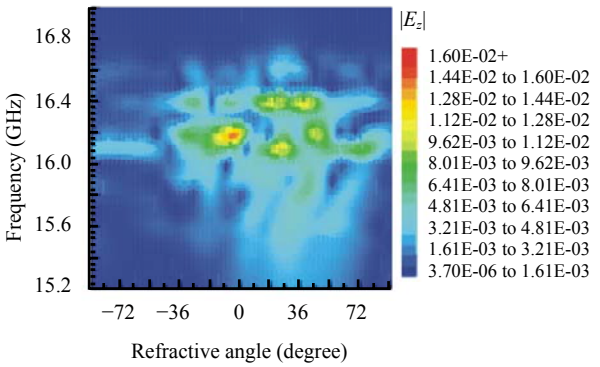

Fig.4 Electric field component $E_z(r, f)$ distribution due to the metamaterial prism

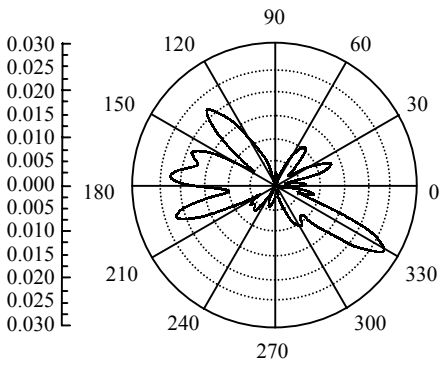

Fig.5 Distribution of electric field component $E_z(r, t)$ in polar plot due to the metamaterial prism at f=16.21 GHz

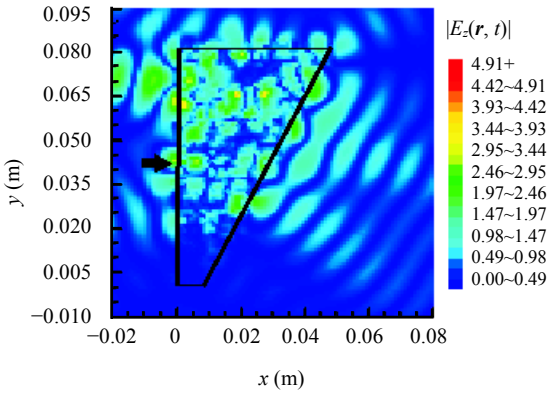

Fig.6 Distribution of electric field componet $E_z(r, t)$ in rectangular linear coordinates around the metamaterial prism at f=16.21 GHz

$$\bar{\boldsymbol{C}}=\begin{bmatrix} \dfrac{\boldsymbol{C}}{\varepsilon_0\varepsilon_h} & 0 \\ 0 & \dfrac{\boldsymbol{C}}{\mu_0} \end{bmatrix}, \tag{7b}$$

$$\boldsymbol{C}=\begin{bmatrix} C_x & 0 & 0 \\ 0 & C_y & 0 \\ 0 & 0 & C_z \end{bmatrix}. \tag{7c}$$

The expressions of elements in the matrix $\boldsymbol{C}$ for a three-dimensional array of dipoles can be obtained in terms of the lattice spacings d_x, d_y, and d_z in the corresponding x-, y-, and z-directions as follows

$$C_x=f\left(\frac{d_y}{d_x},\frac{d_z}{d_x}\right), \tag{8a}$$

$$C_y=f\left(\frac{d_z}{d_y},\frac{d_x}{d_y}\right), \tag{8b}$$

$$C_z=f\left(\frac{d_x}{d_z},\frac{d_y}{d_z}\right). \tag{8c}$$

where

$$f\left(\frac{d_y}{d_x},\frac{d_z}{d_x}\right)=\left(\frac{d_y}{d_x}\right)\left(\frac{d_z}{d_x}\right)\times\left[\frac{1.202}{\pi}-S\left(\frac{d_y}{d_x},\frac{d_z}{d_x}\right)\right]. \tag{9}$$

The function $S\left(\dfrac{d_y}{d_x},\dfrac{d_z}{d_x}\right)$ in Eq.(9) is defined as

$$S\left(\frac{d_y}{d_x},\frac{d_z}{d_x}\right)=\frac{1}{\pi}\sum_{n=-\infty}^{\infty}\sum_{s=-\infty}^{\infty}\sum_{m=1}^{\infty}(2m\pi)^2 \times K_0\left(2m\pi\left[\left(\frac{nd_y}{d_x}\right)^2+\left(\frac{sd_z}{d_x}\right)^2\right]^{1/2}\right), \tag{10}$$

while $K_0(\cdot)$ denotes the modified Bessel function of order 0 so that the terms with n=s=0 are excluded.

From Eq.(6), we notice that the polarizability matrix is an unknown one. To obtain the effective constitutive parameters of the artificial medium, the matrix must be evaluated first. According to Eq.(4), the investigation under six different pairs of incident waves ($\boldsymbol{E}^{\mathrm{i}}$, $\boldsymbol{H}^{\mathrm{i}}$) is needed. For each pair of incident waves, induced electric currents are obtained by using the numerical method first, that is, the MoM. Then the electric and magnetic dipole moments ($\boldsymbol{p}_{\mathrm{e}}$, $\boldsymbol{p}_{\mathrm{m}}$) are evaluated using Eqs.(5a) and (5b), and finally six equations can be obtained. Considering all the six pairs of incident waves for all the components of dipole moments, we have theoretically obtained thirty-six scalar equations to determine the thirty-six elements of the polarizability matrix. In the present analysis, we choose (k_x, E_z), ($-k_x$, E_z), (k_y, E_x), ($-k_y$, E_x), (k_z, E_y) and ($-k_z$, E_y) as six incident plane waves. In the numerical analysis, we disregard the thickness of the inclusion and consider it as a thin perfect conductor. In this case, the EFIE is employed and the MoM with curved parametric quadratic surface and roof-top basis functions (Song and Chew, 1995) are used to obtain the electric currents.

Numerical results

To show the applicability of these formulations, we calculate the effective constitutive parameters of the array fabricated by the cross SRRs, and the results are shown in Fig.8. Geometry of a CSRR under consideration is depicted in Fig.7. It is composed of two perpendicularly intersecting SRRs. Each SRR is made of two aluminum strips (Shelby, 2001). The structure of CSRR is defined by the following parameters: the gap width g=1 mm, the strip width w=0.5 mm, the inner radius r_{in}=2 mm, and the outer radius r_{out}=3 mm. A three-dimensional array synthesized using the CSRRs is shown in Fig.8. The spaces in the corresponding x-, y-, and z-directions are the same and are set as 8 mm.

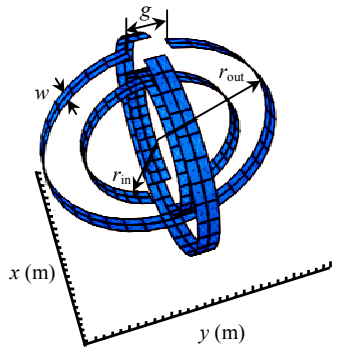

Fig.7 Geometry of a single CSRR where g=1 mm, w=0.5 mm, r_{in}=2 mm, and r_{out}=3 mm

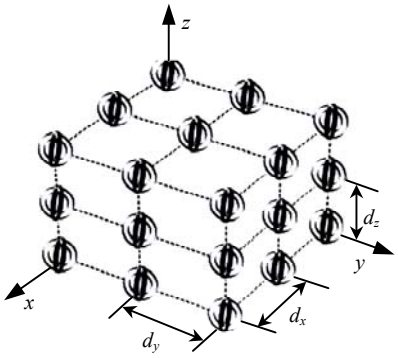

Fig.8 Geometry of a 3D array synthesized using the CSRRs whose d_x=d_y=d_z=8 mm

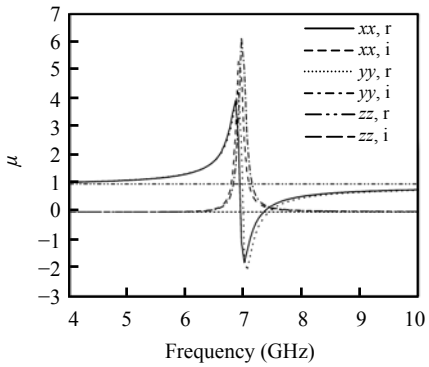

Fig.10 Permeability tensor elements, μ_{xx}, μ_{yy} and μ_{zz}, versus frequency for a 3D array of CSRRs

The effective permittivity tensor elements of ε_{xx}, ε_{yy}, and ε_{zz} are shown in Fig.9, each as a function of frequency. At the same time, Fig.10 depicts the variations of the effective permeability tensor elements of μ_{xx}, μ_{yy} and μ_{zz}, respectively. The other off-diagonal elements are negligibly small according to the numerical data, compared with the diagonal elements. We find from these figures that the real parts of the permeability and permittivity tensor elements ε_{xx}, ε_{yy}, μ_{xx} and μ_{yy} become negative simultaneously from about 6.9 GHz to 7.3 GHz. Also, the *zz*-elements, ε_{zz} and μ_{zz}, are almost constant versus frequency. In particular, we can observe that the values of ε_{xx} and ε_{yy} are almost the same, and so are the values of μ_{xx} and μ_{yy}. This clearly demonstrates the 2-dimensional isotropic features of the metamaterial in the *xoy*-plane. The slight discrepancy found is due to the slightly coarse frequency step. Evidently, this artificial material is characterized by uniaxial anisotropy, and the optical axis is the *z*-axis.

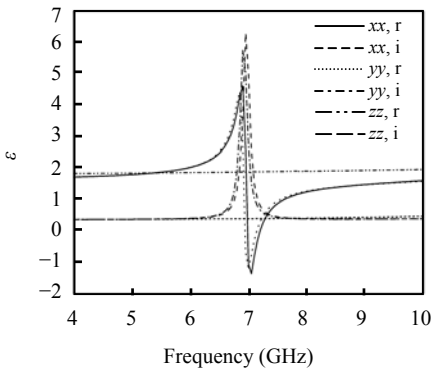

Fig.9 Permittivity tensor elements, ε_{xx}, ε_{yy} and ε_{zz}, versus frequency for a 3D array of CSRRs

TRANSMISSION LINE THEORY

In this section, a periodic SRR array of microscopic nature is considered without loss of generality. When the wavelength is much longer than the inclusion dimensions and lattice spacing, an equivalent continuous material of macroscopic nature can thus be obtained.

Due to the array's periodicity, our analysis begins with single SRR in Fig.11, which does not include the metallic cylinder. In order to obtain magnetic response, we consider the polarization of the incident magnetic field $\boldsymbol{H}^{\mathrm{i}}$ penetrating through this SRR, that is, along the *y*-axis in the present case. The propagation direction $\boldsymbol{k}_0$ and the polarization of the incident electric field $\boldsymbol{E}^{\mathrm{i}}$ are in the *xoz*-plane.

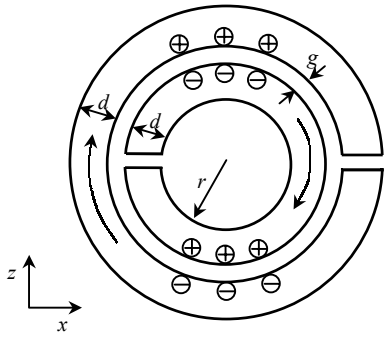

Fig.11 Geometry of a single circle SRR

Taking into account the currents and charges on the surface of two split rings, we can obtain its equivalent circuit model by using the TLT as shown in Fig.12. The magnetic response and conductor loss

of the outer split ring are denoted as L_1A_x and R; C_1A_x with C_p accounting for the capacitances at the splits of the outer and inner rings, respectively. The top C_c represents the capacitance between the upper half of the outer split ring and the upper half of the inner ring; the bottom C_c represents the capacitance between the lower half of the outer split ring and the lower half of the inner ring. Due to the symmetry of the structure they should have the same value, so we use only one capacitance named C_c to define them. In Fig.12, we use two inductances: L_{p1} and L_{p2} and two resistances: r_1 and r_2 to model the magnetic response and conductor loss of the inner ring. That is because the induced currents can flow from the upper half of the outer split ring to the upper half of the inner split ring through the top C_c, and from the lower half of the inner split ring to the lower half of the outer ring through the bottom C_c.

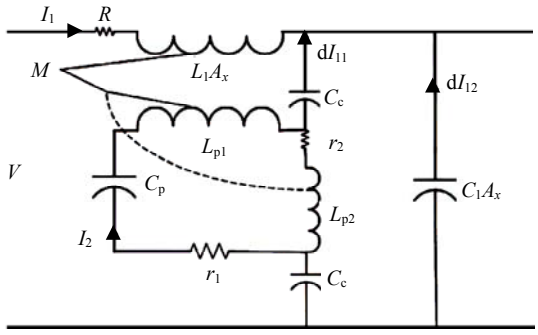

Fig.12 Equivalent circuit of circle SRR in Fig.11

If we introduce metallic cylinders into it, it seems that we have introduced a shunt impedance to L_{p1}, L_{p2} and C_c branches. The values of L_{p1}, L_{p2} and C_c may change, but the analytical model and method does not change. That is why only SRR structures can exhibits both negative permittivity and negative permeability.

By using TLT, the telegrapher equations for the transmission line segment shown in Fig.12 can be formulated as

$$\mathrm{d}V=-\left[I_1(\mathrm{j}\omega L_1A_x+R)+I_2\mathrm{j}\omega M\right], \tag{11a}$$

$$\mathrm{d}I=-\left(\mathrm{j}\omega C_1A_x+\frac{1}{2/(\mathrm{j}\omega C_c)+r_2+\mathrm{j}\omega L_{p2}}\right)V, \tag{11b}$$

where I_2 satisfies the following equations

$$\mathrm{d}I_{11}=\frac{1/(\mathrm{j}\omega C_1A_x)}{1/(\mathrm{j}\omega C_1A_x)+2/(\mathrm{j}\omega C_c)+\mathrm{j}\omega L_{p2}+2r}\mathrm{d}I, \tag{12a}$$

$$I_2(\mathrm{j}\omega L_p+r_p+1/(\mathrm{j}\omega C_p))+I_1\mathrm{j}\omega M-\mathrm{d}I_{11}\mathrm{j}\omega L_{p2}=0. \tag{12b}$$

After re-forming Eqs.(12a) and (12b) to find I_2 as a function of I_1 and V, we substitute I_2 into Eqs.(11a) and (11b). Thus the telegrapher equations can be found as

$$\mathrm{d}V=-\mathrm{j}\omega A_x\left[\left(1-\frac{\mathrm{j}R}{\omega L_1A_x}-\frac{\boldsymbol{k}^2}{1-\omega_p^2/\omega^2-\mathrm{j}r_p/(\omega L_p)}\right)\times L_1I_1+\frac{\mathrm{j}M/(L_pA_x\omega)}{(1-\omega_p^2/\omega^2-\mathrm{j}r_2/(\omega L_{p2}))}\times\frac{V}{(1-2\omega_{p2\,c}^2/\omega^2-\mathrm{j}r_p/(\omega L_p))}\right], \tag{13a}$$

$$\mathrm{d}I=-\mathrm{j}\omega C_1A_xV\times\left(1+\frac{1}{2C_1A_x/C_c-\omega^2/\omega_{p2\,c}^2+\mathrm{j}\omega C_1A_xr_2}\right), \tag{13b}$$

where $L_p=L_{p1}+L_{p2}$, $r_p=r_1+r_2$ for the case of SRRs without rods, $\mathrm{d}I=\mathrm{d}I_{11}+\mathrm{d}I_{12}$, $\omega_p=1/\sqrt{L_pC_p}$, $\omega_{p2\,c}=1/\sqrt{L_{p2}C_c}$, $\boldsymbol{k}^2=M^2/(L_pL_1A_x)$ and M is the mutual inductance between the inner split ring and the outer one (in other words, it is the mutual inductance between L_1A_x and L_p). Thereby based on the correspondence between the telegrapher equations and the Maxwell's equations, the effective constitutive parameters can be easily extracted from these two equations

$$\mu_{\mathrm{eff}}=L_1\left(1-\frac{\mathrm{j}R}{\omega L_1A_x}-\frac{\boldsymbol{k}^2}{1-\omega_p^2/\omega^2-\mathrm{j}r_p/(\omega L_p)}\right), \tag{14a}$$

$$\varepsilon_{\mathrm{eff}}=C_1\left(1+\frac{1}{2C_1A_x/C_c-\omega^2/\omega_{p2\,c}^2+\mathrm{j}\omega C_1A_xr_2}\right), \tag{14b}$$

$$\varsigma_{\text{eff}}=\frac{\mathrm{j}M/(L_{\text{p}}A_x\omega)}{(1-\omega_{\text{p}}^2/\omega^2-\mathrm{j}r_2/(\omega L_{\text{p2}}))}\times\frac{1}{(1-2\omega_{\text{p2 c}}^2/\omega^2-\mathrm{j}r_{\text{p}}/(\omega L_{\text{p}}))}, \tag{14c}$$

$$\xi_{\text{eff}}=0. \tag{14d}$$

It is noticed here that a single SRR can still have negative permittivity, and this agrees with the conclusion drawn from another approach (Ishimaru *et al.*, 2003), which is shown in the later section.

According to the polarization directions of $\boldsymbol{E}^{\text{i}}$ and $\boldsymbol{H}^{\text{i}}$, the tensor expression of constitutive parameters for 1D metamaterial constructed by this type of SRRs and metallic cylinders are given by

$$\bar{\boldsymbol{\mu}}=\begin{pmatrix}1&0&0\\0&\mu_{\text{eff}}&0\\0&0&1\end{pmatrix}, \tag{15a}$$

$$\bar{\boldsymbol{\varepsilon}}=\begin{pmatrix}1&0&0\\0&1&0\\0&0&\varepsilon_{\text{eff}}\end{pmatrix}, \tag{15b}$$

$$\bar{\boldsymbol{\varsigma}}=\begin{pmatrix}0&0&0\\0&0&\varsigma_{\text{eff}}\\0&0&0\end{pmatrix}, \tag{15c}$$

$$\bar{\boldsymbol{\xi}}=\begin{pmatrix}0&0&0\\0&0&0\\0&\xi_{\text{eff}}&0\end{pmatrix}. \tag{15d}$$

Similarly, those for 2D structures are given by

$$\bar{\boldsymbol{\mu}}=\begin{pmatrix}\mu_{\text{eff}}&0&0\\0&\mu_{\text{eff}}&0\\0&0&1\end{pmatrix}, \tag{16a}$$

$$\bar{\boldsymbol{\varepsilon}}=\begin{pmatrix}1&0&0\\0&1&0\\0&0&\varepsilon_{\text{eff}}\end{pmatrix}, \tag{16b}$$

$$\bar{\boldsymbol{\varsigma}}=\begin{pmatrix}0&0&\varsigma_{\text{eff}}\\0&0&\varsigma_{\text{eff}}\\0&0&0\end{pmatrix}, \tag{16c}$$

$$\bar{\boldsymbol{\xi}}=\begin{pmatrix}0&0&0\\0&0&0\\\xi_{\text{eff}}&\xi_{\text{eff}}&0\end{pmatrix}. \tag{16d}$$

So far, we have demonstrated how to obtain the constitutive relations of an artificial material constructed by SRRs. This is an alternative approach as compared to the existing one (Yao *et al.*, 2004). To demonstrate the validity of these formulas, we consider a periodic SRR array. The geometry and dimensions are taken from (Ishimaru *et al.*, 2003) and reproduced in Fig.11. Then we synthesized them into a homogeneous dielectric material whose ε_{r}=4.5. The dimensions of the single SRR are d=0.8 mm, g=0.2 mm, and r=1.5 mm. Here, we assume the SRR to be made of thin perfect conductors. In this case, the values of the corresponding capacitances and inductances in the model can be estimated by a quasi-static approach and by using conformal mapping theory. In our case, we estimate them approximately by using the microstrip line theory.

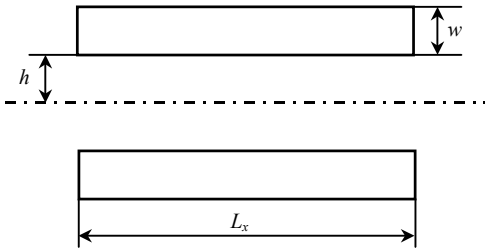

Fig.13 Geometry of two thin coplanar strips each with a capacitance per unit length

An approximate expression for the coupling capacitor between two vertical strip lines in Fig.13 is obtained as

$$C=\frac{\varepsilon K\sqrt{1-g^2}}{K(g)}L_x, \tag{17}$$

where $g=h/(h+w)$, while $K(\cdot)$ denotes the complete elliptic integral defined by

$$K(g)=\int_0^{\pi/2}\frac{\mathrm{d}\phi}{\sqrt{1-g^2\sin^2\phi}}. \tag{18}$$

Thus C_p and C_c can be estimated in this way. As we know, C_1 is comprised of two parts, one is the capacitance of the split, while the other is the parasitic capacitance due to the discontinuity of the structure. The discontinuity part (defined as C_g) is estimated as the capacitance of the gap between microstrip lines. The corresponding formulas are given (Garg *et al.*, 2001) below:

(1) For ε_r=9.6,

$$C_g(9.6)=12\left(\frac{D_{gap}}{W}\right)^m e^{k}W \quad (pF), \tag{19}$$

where

$$m=\begin{cases} 0.8675, & 0.1\le\dfrac{D_{gap}}{W}\le 0.5 \\ 1.565/[(W/t)^{0.16}]-1, & 0.5<\dfrac{D_{gap}}{W}\le 1 \end{cases}$$
$$k=\begin{cases} 2.043(W/t)^{0.12}, & 0.1\le\dfrac{D_{gap}}{W}\le 0.5 \\ 1.97-0.03/(W/t), & 0.5<\dfrac{D_{gap}}{W}\le 1 \end{cases} \tag{20}$$

(2) For 2.5≤ε_r≤15,

$$C_g(\varepsilon_r)=1.167C_g(9.6)(\varepsilon_r/9.6)^{0.9}, \tag{21}$$

where W denotes the effective width of the SRR, D_{gap} represents the gap distance between two SRR rings and t stands for the distance of the SRR from ground. Similarly, the inductances are estimated as follows:

$$L_p=\frac{\mu_0\pi r^2}{2d}. \tag{22}$$

Based on the current distribution on the SRR, we have L_{p1}=L_{p2}=L_p/2. The mutual inductance index is calculated using k^2=S_{in}/S_{out}, where S_{in} and S_{out} denote areas of the inner and outer split rings. The real parts of effective permittivity and permeability values versus frequency are shown in Fig.14. In these figures, the solid curves are obtained from numerical simulations carried out based on the quasi-static Lorentz theory (Yao *et al.*, 2004), and the dashed curves represent the results obtained using the present TLT approach. From this comparison, it is seen that good agreement in variation is achieved.

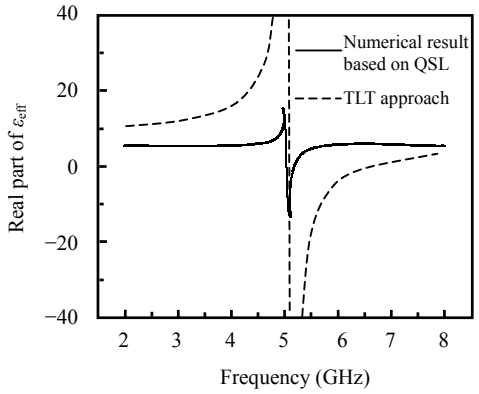

(a)

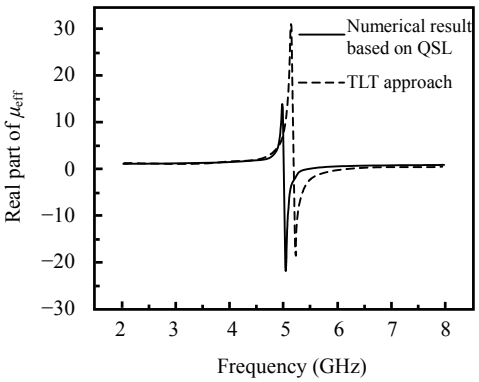

(b)

Fig.14 Comparison of the real parts of ε_{eff} and μ_{eff} of the SRR-constructed materials obtained from simulations based on the QSL theory and the present TLT approach. (a) Effective permittivities; (b) Effective permeabilities

DESIGN PROCEDURE

In this section, we focus on the design of the metamaterials. We make use of periodical array synthesized by the modificative transmission line model to obtain the magnetic properties (Xu *et al.*, 2004a; 2004b). Equivalent TLT was applied to find the effective inductance L_{eq} and capacitance C_{eq} per unit length. Moreover, the S_{21} parameter of this metamaterials was figured out to show that a pass band occurred when the equivalent permittivity and permeability are negative simultaneously. Some special phenomena are shown for further validity.

Single resonant frequency structure

First, we discuss a segment of the transmission line model shown in Fig.15a, which consists of a circular spiral inductor and a metallic cylinder. Use of equivalent TLT yielded an equivalent model as shown in Fig.15b. The effective inductance L_{eq} and capacitance C_{eq} per unit length of the periodically arranged transmission line are given by

$$L_{eq}=L_1\left[\frac{1}{1-\omega^2/\omega_1^2}\right], \tag{23}$$

$$C_{eq}=C_2\left(1-\frac{\omega_2^2}{\omega^2}\right), \tag{24}$$

where $\omega_1=1/\sqrt{L_1C_1}$ and $\omega_2=1/\sqrt{L_2(C_2d_x)}$. Their conversion to the equivalent permeability μ_{eq} and permittivity ε_{eq} yields

$$\mu_{eq}=\frac{L_1}{d_x}\left[\frac{1}{1-\omega^2/\omega_1^2}\right], \tag{25}$$

$$\varepsilon_{eq}=C_2\left(1-\frac{\omega_2^2}{\omega^2}\right). \tag{26}$$

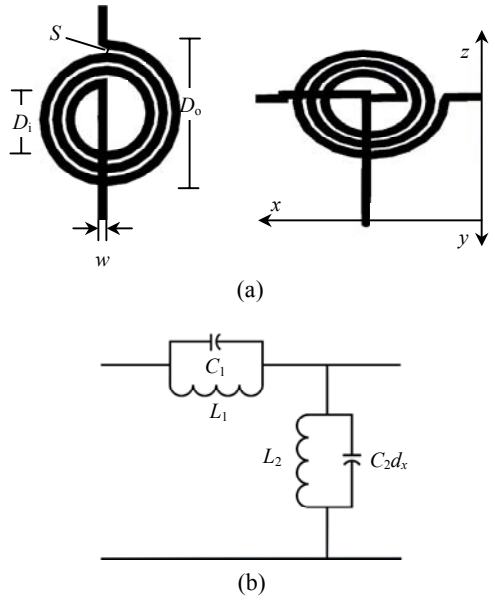

Fig.15 Single resonant frequency structure and its equivalent transmission line model. (a) Unit structure of single resonant structure; (b) Its equivalent transmission-line model

In Eqs.(25) and (26), the values of L_1, L_2, C_1 and C_2 must be determined separately, and their values can be estimated by a quasi-static approach (Gupta, 1996) and expressed as follows

$$L_1=0.03937\frac{a^2n^2}{8a+11c}k_g \quad \text{(nH)}, \tag{27a}$$

$$L_2=\mu_0 d_z\frac{\ln(d_x/r)}{2\pi}, \tag{27b}$$

$$C_1=3.5\times10^{-5}D_o+0.06 \quad \text{(pF)}, \tag{27c}$$

$$C_2d_x=\frac{\varepsilon_0\pi D_o^2}{4d_z}, \tag{27d}$$

in which, $a=(D_o+D_i)/4$ (μm), $c=(D_o-D_i)/2$ (μm), $k_g=0.57-0.145\ln(w/d_z)$ (when $w/d_z>0.05$), and n denotes the number of turns of the spiral inductor.

Therefore, the equivalent permeability and relative permittivity versus frequency can be calculated and the variation is shown in Fig.16. Here, the dimensions of the spiral inductor are n=2, D_o=6 mm, S=0.1 mm, and w=0.2 mm. The radius r of the metallic cylinder is 0.2 mm, and its length L_z=9.6 mm. The lattice spaces are d_x=10 mm, d_y=0.2 mm, and d_z=10 mm. The frequency band ranged between ω_1 and ω_2 is observed. Two-dimensional isotropic metamaterials can be formed by periodically extending this unit inclusion, as shown in Fig.17. However, if ω_2 is much larger than ω_1, the absolute value of μ_{eq} may change very slightly when the frequency approaches ω_2. Furthermore, the change of μ_{eq} versus the frequency is very fast. In practice, we usually need a relatively constant μ_{eq} in some frequency band. A double magnetic resonant frequency

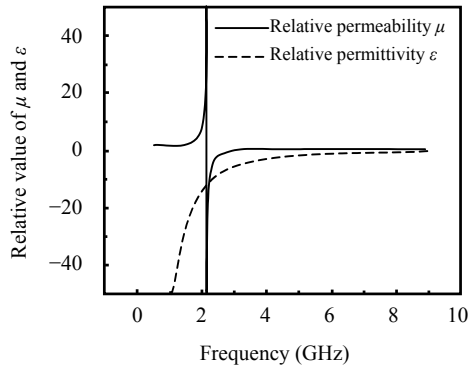

Fig.16 Theoretical value of μ and ε of single resonant frequency structure

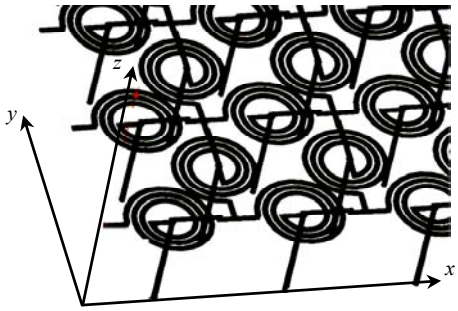

Fig.17 Array structure made of single resonant frequency unit

structure is presented here to overcome these problems and achieve broader bandwidth and better performance.

Double resonant frequency structure

1. Circular spiral inductor together with rectangular SRR

Here, we modify the single magnetic resonant inclusion into a double one by inserting a rectangular SRR, which is shown in Fig.18a. The corresponding equivalent transmission line model is shown in Fig.18b. As in the analysis given above, we have

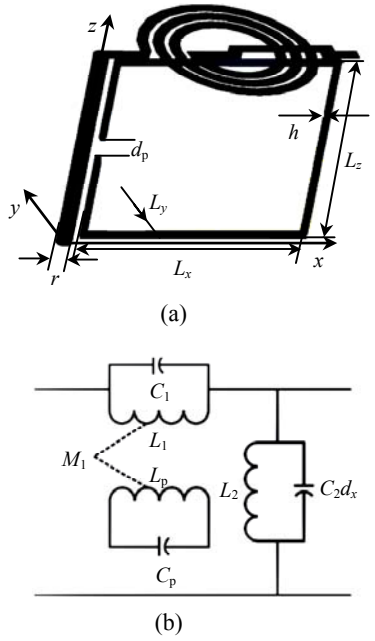

Fig.18 A unit of double resonant frequency structure and its equivalent transmission line model. (a) A double resonant frequency unit; (b) Its equivalent transmission line model

$$L_{eq}=L_1\left[\frac{1}{1-\omega^2/\omega_1^2}-\frac{\boldsymbol{k}_1^2}{(1-\omega^2/\omega_1^2)(1-\omega_p^2/\omega_1^2)}\right], \quad (28)$$

where $\omega_p=1/\sqrt{L_pC_p}$, and $\boldsymbol{k}_1=M_1^2/[L_p(L_1d_x)]$, which denotes the coupling index of the spiral inductor and the ring resonator. Similarly, the equivalent capacitance is given by

$$C_{eq}=C_2(1-\omega_2^2/\omega^2). \quad (29)$$

Substituting them into the definition of permeability μ_{eq} and permittivity ε_{eq} respectively, yields

$$\mu_{eq}=\frac{L_1}{d_x}\left[\frac{1}{1-\omega^2/\omega_1^2}-\frac{\boldsymbol{k}_1^2}{(1-\omega^2/\omega_1^2)(1-\omega_p^2/\omega^2)}\right], \quad (30)$$

$$\varepsilon_{eq}=C_2(1-\omega_2^2/\omega^2), \quad (31)$$

and

$$L_p=\frac{\mu_0 S_{loop}}{d_y}, \quad (32)$$

$$C_p=\frac{\varepsilon_0 S_{eff}}{d_p}, \quad (33)$$

in which, S_{loop} represents the area of the loop resonator, and S_{eff} stands for the effective area of the split. Analysis showed that the values of mutual inductances do not affect results much. Then $\boldsymbol{k}_1$ is evaluated approximately by $\boldsymbol{k}_1=S_{loop}/(d_xd_z)$.

The dimensions of the rectangular SRR are L_z=9.4 mm, L_y=h=0.2 mm, d_p=0.4 mm, and S_{eff}=1.5L_yh. The variations of the μ_{eq} and ε_{eq} versus the frequency are shown in Fig.19. The absolute value of μ is roughly doubled in the whole frequency region compared to the previous case, which obviously extends the bandwidth with the simultaneously negative permittivity and permeability.

Next, we form upper and lower symmetrical arrays by just using the circular spiral inductor and place it into a waveguide, as shown in Fig.20. In this example, the dimensions of the waveguide are 60 mm×70 mm×3.002 mm, and the other dimensions labelled in Fig.18a are the same as those above except

for n=3 and D_o=6.8 mm. As we can see from Fig.20, the spiral inductor array is located in the middle of the waveguide. We have to point out that there are two incident wave ports–the upper and the lower ones, and that the integration line of the upper one points from the upper PEC plate of the waveguide to the middle spiral plane; the integration line of the lower one points from the ground plate of the waveguide to the middle spiral plane (with the same definitions of the output ports). In this way, the spiral inductors can have effect on the field. In other words, the fields on the spiral inductor produced by the upper part and lower part of the waveguide will compensate each other.

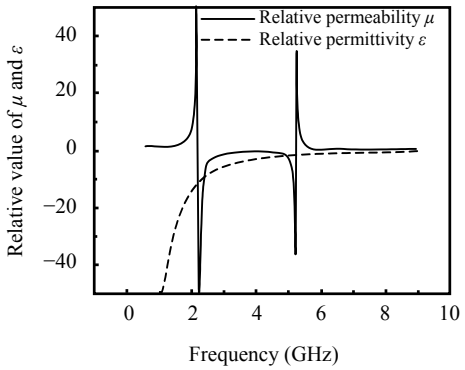

Fig.19 Theoretical value of μ and ε of double resonant frequency structure

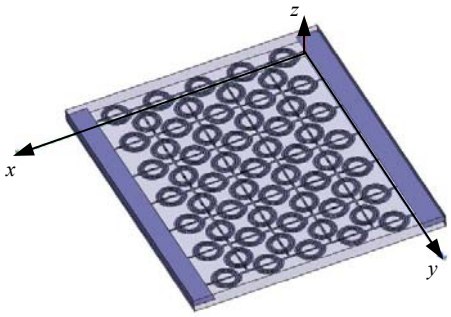

Fig.20 Model with a negative μ_{eq} and positive ε_{eq}

From the analysis above, this artificial material has a negative μ_{eq} and positive ε_{eq} in a certain wave band. The effective S_{21} parameter simulated by commercial software, Ansoft HFSS, is given in Fig.21. The observed stop band in this figure means that electromagnetic waves cannot pass through the materials with $+\varepsilon$ and $-\mu$.

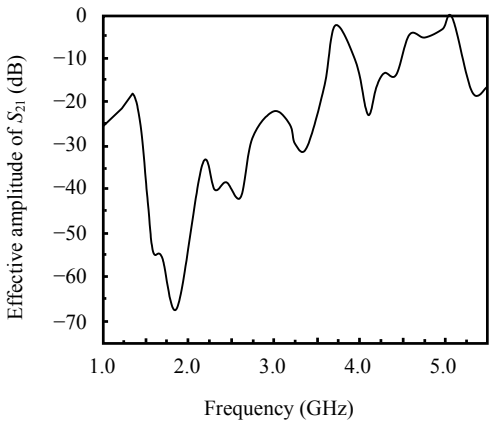

Fig.21 The simulation amplitude of S_{21} parameter of the structure in Fig.20

To show the properties of the metamaterials with simultaneously negative permittivity and permeability, we introduce the double split rings into the model in the following case. The new model is shown in Fig.22 and placed into the same waveguide. In this case, some rectangular rods (0.2 mm×0.2 mm) are

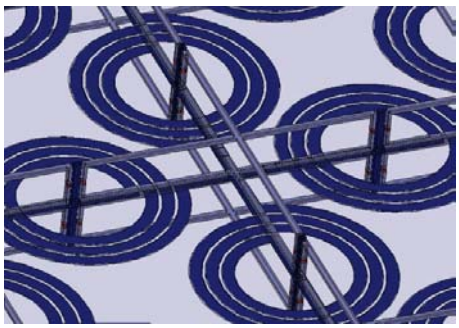

(a)

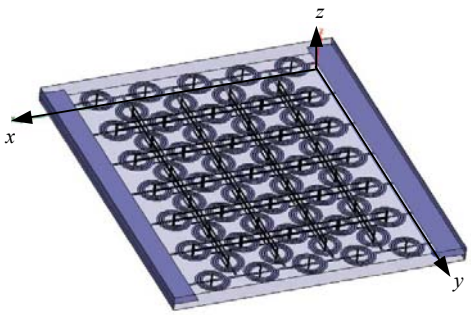

(b)

Fig. 22 Double resonant frequency left-handed material model. (a) Close view of the model; (b) Overall view of the model

added in it. In Fig.22a, we filled natural dielectric materials into the splits of the rectangular rings. The resonant frequency of the SRR can be adjusted by changing the value of its permittivity. Here, we set ε to be 15. The simulation result of S_{21} is given in Fig.23. By comparing the results of Fig.21 and Fig.23, we can observe that the pass band due to the double negative parameters becomes broader, which means a relatively constant negative μ_{eq} has been achieved.

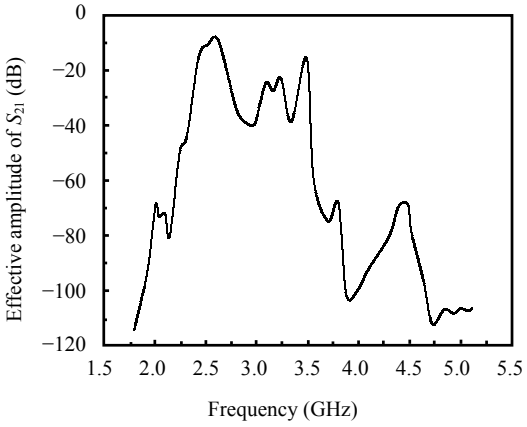

Fig.23 The simulation amplitude of S_{21} parameter of the structure in Fig.22

2. Coupled strip line together with rectangular SRR

The proposed DNM periodic structure of open type is shown in Fig.24 and its unit cell is shown in Fig.25. The unit cell is made up of 4-inclusions shown in Fig.26 by sweeping the inclusion around the via or the z-axis. The inclusion consists of a broadside coupled strip line with a via connected to the ground and a split resonant ring. The broadside coupled strip line, the via and the ground line form the outer ring, and it will have magnetic mutual coupling with the inner split ring. The magnetic coupling is essential for the negative permeability, and this can be seen in the following.

The equivalent circuit of an inclusion is shown in Fig.27. The outer ring and the inner ring account for the inductances L_1A_x and L_p, respectively. L_2 is due to the via, and C_2A_x is the capacitance between the broadside strip line and the ground. C_p is the capacitance at the split of the inner ring. Here we only deal with lossless case for simplicity although the loss can also be included.

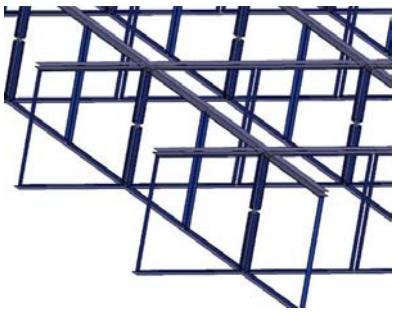

Fig.24 Periodic DNM structure

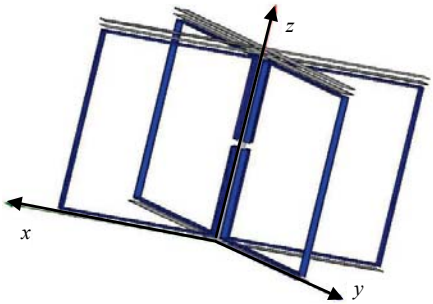

Fig.25 A unit cell of the structure shown in Fig.24

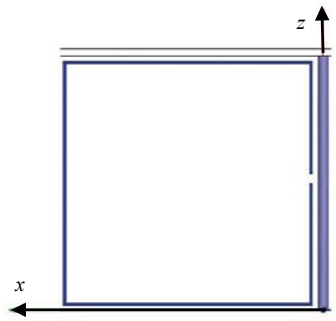

(a)

(b)

Fig.26 An inclusion of the structure shown in Fig.25. (a) Side view of an inclusion; (b) Another view of the inclusion

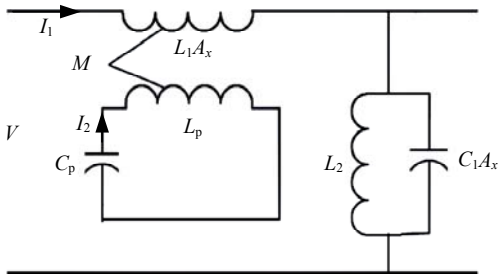

Fig.27 Equivalent circuit model of an inclusion shown in Fig.26

The telegrapher's equations for the transmission line segment shown in Fig.27 can be easily derived.

$$\mathrm{d}V=-(I_1\mathrm{j}\omega L_1A_x+I_2\mathrm{j}\omega M), \tag{34}$$

$$\mathrm{d}I=-[1/(\mathrm{j}\omega L_2)+\mathrm{j}\omega C_1A_x]V, \tag{35}$$

$$I_2(\mathrm{j}\omega L_\mathrm{p}+1/(\mathrm{j}\omega C_\mathrm{p}))=0\,. \tag{36}$$

Thus, we further have

$$\mathrm{d}V=-\mathrm{j}\omega L_1A_xI_1\left(1-\frac{M^2/L_\mathrm{p}L_1A_x}{1-\omega_\mathrm{p}^2/\omega^2}\right), \tag{37}$$

$$\mathrm{d}I=-\mathrm{j}\omega C_1A_xV(1-\omega_1^2/\omega^2), \tag{38}$$

where $\omega_1=1/\sqrt{L_2C_1A_x}$ and $\omega_\mathrm{p}=1/\sqrt{L_\mathrm{p}C_\mathrm{p}}$.

Then using the relation between telegrapher's equation and Maxwell equation, we can extract the parameters as follows:

$$\mu_\mathrm{eff}=\frac{L_1}{\mu_0}\left(1-\frac{\boldsymbol{k}^2}{1-\omega_p^2/\omega^2}\right), \tag{39a}$$

$$\varepsilon_\mathrm{eff}=\frac{C_1}{\varepsilon_0}\left(1-\frac{\omega_1^2}{\omega^2}\right), \tag{39b}$$

$$\varsigma_\mathrm{eff}=0\,, \tag{39c}$$

$$\xi_\mathrm{eff}=0\,, \tag{39d}$$

where $\boldsymbol{k}=M^2/(L_\mathrm{p}L_1A_x)$. Although our design and analysis are mainly based on circuit theory, this structure is essentially compatible with TEM, TE and TM modes and can be excited easily by waveguide or microstrip line.

MAGNETIC RESPONSE ANALYSIS OF A UNIT CELL

To demonstrate the double negative property of the structure in Fig.28, we first analyze a unit cell in HFSS (ANSOFT).

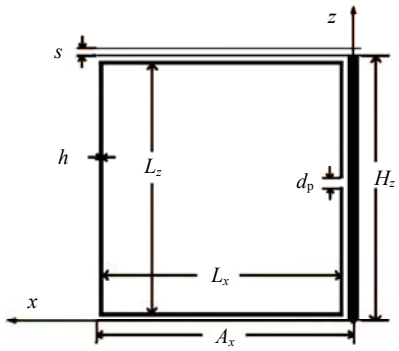

(a)

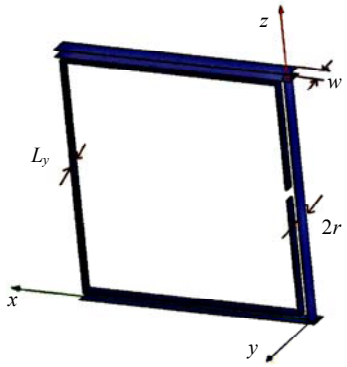

(b)

Fig.28 Dimensions of the inclusion. (a) Side view; (b) 3D view

As shown in Fig.29, we put a unit cell in a waveguide (20 mm×19.9 mm×10.5 mm). The dimensions of the unit structure are: A_x=9.9 mm, H_z=10 mm, w=0.8 mm, s=0.2 mm, d_p=0.4 mm, r=0.2 mm, L_x=9.2 mm, L_y=0.4 mm, L_z=9.6 mm, and h=0.1 mm (in this paper, all the structures will be formed by this-sized unit cell). The boundary and excitation conditions are assumed as follows: PEC for top and bottom walls; PMC for right and left walls; TEM wave transport in y-direction with $\boldsymbol{E}$ in z-direction; a PML at the end of the waveguide and all the structures in this model are made of copper.

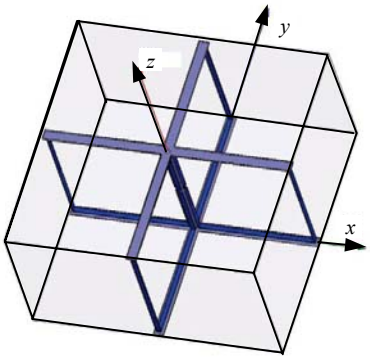

Fig.29 A unit cell in waveguide

Then we analyze this model at three frequency points. The first one is 6.2 GHz, which is in the paramagnetism region; the second one is 8.4 GHz, which is in the antimagnetism and double negative material region; the third one is 9 GHz, which is in the antimagnetisim but positive μ region. Fig.30 and Fig.31 show the sketched magnetic dipoles and electric field distributions. At 6.2 GHz, the equivalent magnetic dipole is in the same direction as that of the incident wave and it strengthens the field, so this is in the positive effective permeability region. At 8.4 GHz, the equivalent magnetic dipole and the ***E*** field near the body of the structure are in direction opposite to that of the incident wave, which changes the field distribution a lot. Although only based on this phenomenum we cannot decide the sign of the permeability, we can combine it with other results to determine the characteristic of this material, for example the negative refraction phenomenum as we will do in the following section. As for the case of 9 GHz, although the equivalent magnetic dipole is in the opposite direction of the incident wave, it does not change the whole field distribution as much as in the case of 8.4 GHz. It is just these equivalent dipoles that determine the properties of this structure, and this provides another approach for examining a design in general.

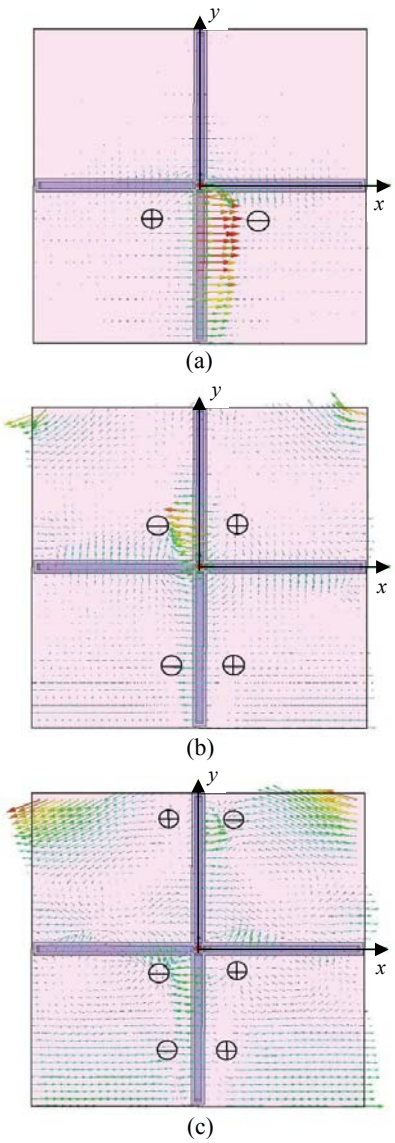

Fig.30 *H*-field distributions in a unit cell structure at different frequency regions, and the equivalent magnetic dipoles. (a) 6.2 GHz and phase 0°; (b) 8.4 GHz and phase 0°; (c) 9 GHz and phase 0°

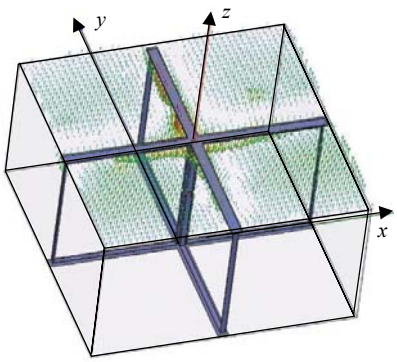

Fig.31 *E* field distribution at 8.4 GHz and phase 0°

NEGATIVE REFRACTION PHENOMENON

In order to further demonstrate the double negative index property of the proposed structure, a prism is designed and put into a waveguide (120 mm×100 mm

×10.5 mm) as shown in Fig.32. Here the waveguide is used for two reasons: (1) most experiments and simulations concern about DNM are in waveguide; and (2) it is used to feed the structure better and to reduce the computational time. Then it is excited by the dominant mode of the waveguide (TE_{10}). Since we know that the unit cell of this structure has strong antimagnetism property, so we can further explore this structure at 8.4 GHz. After full-wave analysis, we saw a very good negative refraction phenomenon (Fig.33), with refraction angle of about −40°. The black arrows in Fig.33 show the wave propagation direction after refraction, and these arrows are drawn based on the animation and Poynting vector given by HFSS.

CONSTRUCTION OF THE NRI LENS

A planar negative refraction index lens is constructed and put into a waveguide as shown in Fig.34a, and two PMLs are set at the two ports of the waveguide. Then a current is introduced into the copper cylinder as the incident source. The operating frequency is chosen at 8.4 GHz, which was also used in the previous work (Xu *et al.*, 2004a; 2004b). The dimension of the waveguide is 100 mm×140 mm ×10.5 mm. Simulation is also done by using the HFSS package, and the field distribution is shown in Fig.34b. As seen from the simulation results, the wave refocuses after passing through the negative refraction index lens, which again demonstrates the double negative index property of this structure at 8.4 GHz.

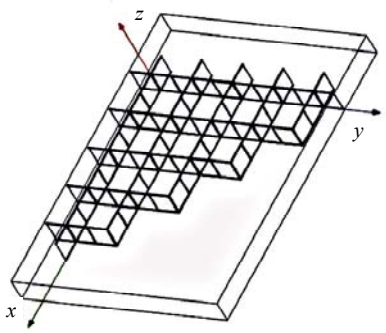

Fig.32 The prism in waveguide, which is used to observe the negative refraction phenomena

LOSS DISCUSSION

The structure is made of copper, a theoretically perfect conductor. In our simulations or future fabrication, we will add imaginary parts into the effective parameters μ_{eff} and ε_{eff} in Eq.(39), then energy loss is for sure produced. We designed a rectangular slab using the unit cell and put it in the waveguide (100 mm×100.8 mm×10.5 mm), shown in Fig.35. *S*-parameters are observed to see the energy loss and the results near the double negative index region are shown in Table 1. These *S*-parameters indicate that at the double negative index region the energy loss of the structure fed by a waveguide is smaller compared to the traditional SRR structure whose S_{21} falls within −7 dB to −10 dB (Moss *et al.*, 2002).

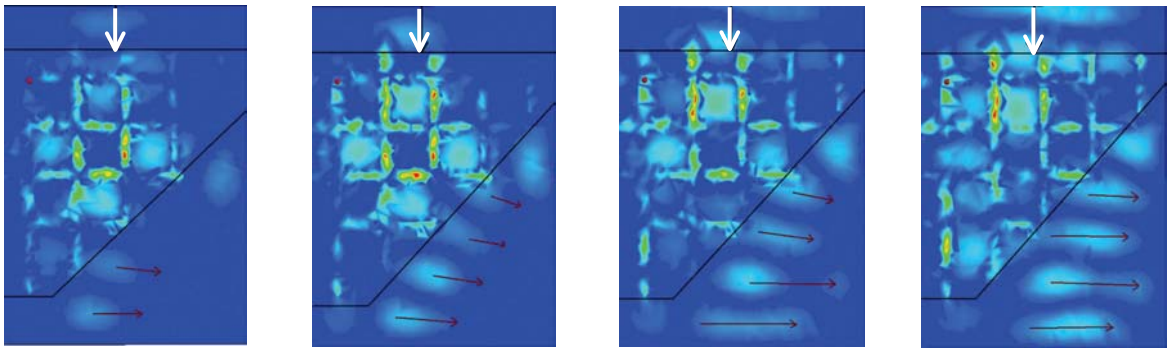

Fig.33 Negative refraction in LHM or DNM prism made of our proposed structure. The black arrows indicate the wave propagation direction after refraction. (a) Phase 90°; (b) Phase 125°; (c) Phase 145°; (d) Phase 160°

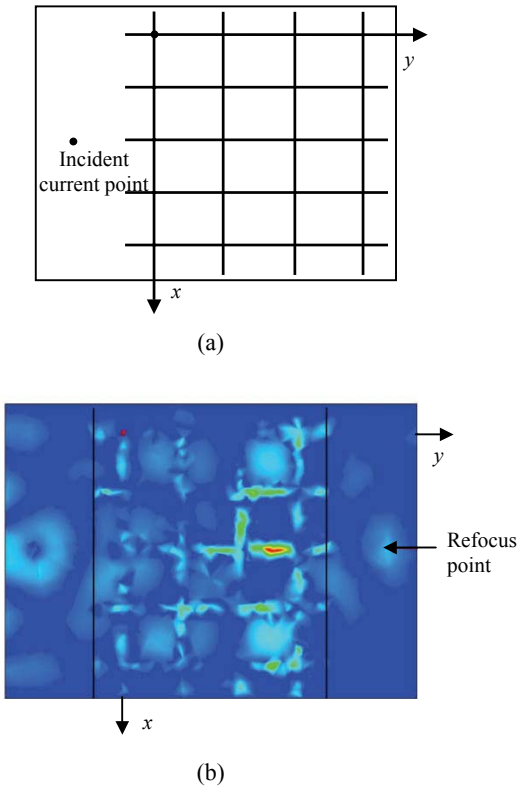

Fig.34 Construction of NRI lens. (a) Planar distributed NRI lens; (b) *E* field distribution of the NRI lens at 8.4 GHz, phase 50° simulated by the HFSS package

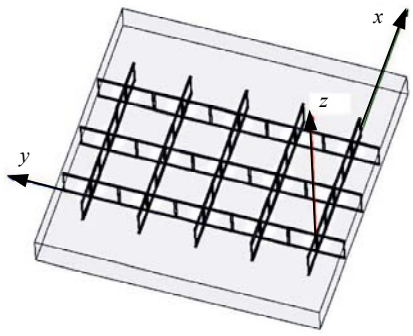

Fig.35 A 59.4 mm thick DNM slab in waveguide

Table 1 *S*-parameters of structure in Fig.35

Frequency (GHz)	S_{21} (dB)	S_{11} (dB)
8.2	−2.0	−25
8.3	−1.5	−13
8.4	−2.0	−9

NEGATIVE PERMEABILITY OVER DOUBLE FREQUENCY BANDS

Fig.36 shows the double resonant frequency structure constructed by using a spiral inductor and a split ring which is loaded inside. We analyzed it using the transmission line model, and the equivalent circuit model is shown in Fig.37. The outer spiral inductor accounts for the parallel resonant circuit consisting of L_1 and C_1, and the inner split ring accounts for the series resonant circuit consisting of L_p and C_p. C_2A_x is the shunt capacitor of a unit, and C_s is the capacitance between two unit structures. From this figure, we find that the outer spiral inductor provides one resonant frequency point, while the inner split ring provides the other resonant frequency point.

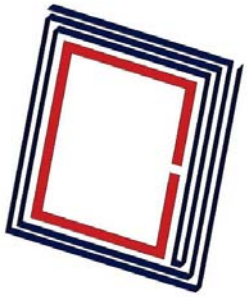

Fig.36 A unit of the double resonant frequency structure

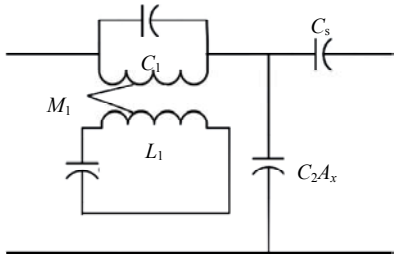

Fig.37 Equivalent circuit model of the double resonant frequency structure

We also numerically evaluated the SCS of a unit structure to find the resonant frequency, which is shown in Fig.38. From this figure, two resonant frequency points are observed to confirm the double resonant characteristics.

By using the quasi-static Lorentz theory, we treat this structure as magnetic dipole and calculated the magnetic polarization parameter. In fact second order approximation is made here, and the simulation result of the permeability of this structure is shown in Fig.39. We calculate it at each 50 MHz frequency point.

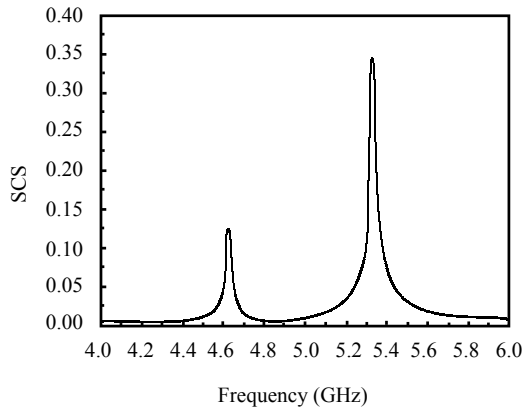

Fig.38 Scattering cross section (SCS) versus frequency for a unit structure

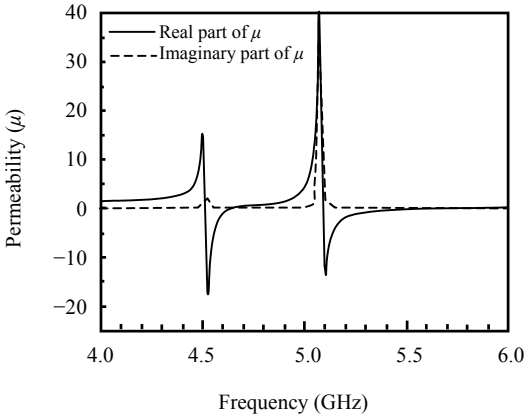

Fig.39 Numerical extraction of the permeability of the double resonant frequency structure

The simulation results revealed that the imaginary part of the effective permeability is extraordinarily small at the first negative permeability region. If we add metallic rods inside to provide the negative permittivity, we can form a double negative materials (DNM) with a low loss property compared to the traditional SRR structures. Still this structure can easily form 3D isotropic DNM with its unit structure arranged on a cube.

CONCLUSION

In this review paper based on some recent work done at the National University of Singapore, we have observed the special propagation properties when the electromagnetic waves pass through a metamaterial sample, which is periodically synthesized by conducting elements. Negative refraction from a prism and image effect from a slab are clearly observed. Natural materials do not give such a possibility. Integral equation method with a fast solver is applied for efficient calculation. Two methods, which are developed based on the quasi-static Lorentz theory and TLT respectively, to determine the effective constitutive parameters of the metamaterials are introduced. The numerical results for the 2D isotropic cross SRR array and 1D SRR array have been shown to validate the applicability. Finally, a detailed design process based on the TLT is presented, which offers a good but simple approach for constructing metamaterials with wide frequency passband and low loss. Moreover, some novel metamaterial examples, which are synthesized by periodically arranged mixtures of microstrip lines/devices, a metallic cylinder/rectangular rod, and a rectangular SRR, are brought forward. The simulation results obtained from HFSS software are given to verify the feasibility of this design, although there are no experimental results for comparison purpose.

References

Caloz, C., Sanada, A., Itoh, T., 2004. A novel composite right-/left-handed coupled-line directional coupler with arbitrary coupling level and broad bandwidth. *IEEE Trans. Microwave Theory Tech.*, **52**(3):980-992. [doi:10.1109/TMTT.2004.823579]

Chen, H.S., Ran, L.X., Huangfu, J.T., Zhang, X.M., Chen, K.S., Grzegorczyk, T.M., Kong, J.A., 2003. T-junction waveguide experiment to characterize left-handed properties of metamaterials. *Journal of Applied Physics*, **94**(6):3712-3716. [doi:10.1063/1.1603344]

Collin, R.E., 1991. Field Theory of Guided Waves. IEEE Press, New York, Chapter 12.

Eleftheriades, G.V., Iyer, A.K., Kremer, P.C., 2002. Planar negative refractive index media using periodically L-C loaded transmission lines. *IEEE Trans. Microwave Theory and Techniques*, **50**(12):2702-2712. [doi:10.1109/TMTT.2002.805197]

Engheta, N., 2003. Metamaterials with negative permittivity and permeability: background, salient features, and new trends. *Microwave Symposium Digest, 2003 IEEE MTT-S International*, **1**:187-190. [doi:10.1109/MWSYM.2003.1210912]

Falcone, F., Martin, F., Bonache, J., Marques, R., Lopetegi, T., Sorolla, M., 2004. Left-handed coplanar waveguide band pass filters based on bi-layer split ring resonators. *IEEE Microwave and Wireless Components Letters*, **14**(1):10-12. [doi:10.1109/LMWC.2003.821512]

Garg, R., Bhartia, P., Bahl, I., Ittipiboon, A., 2001. Microstrip

Antenna Design Handbook. Artech House, Boston and London.

Gay-Balmaz, P., Martin, O.J.F., 2001. Efficient isotropic magnetic resonators. *Applied Physics Letters*, **81**(5):939-941. [doi:10.1063/1.1496507]

Gay-Balmaz, P., Martin, O.J.F., 2002. Electromagnetic resonances in individual and coupled split ring resonators. *Journal of Applied Physics*, **92**(5):2929-2936. [doi:10.1063/1.1497452]

Grbic, A., Eleftheriades, G.V., 2003. Dispersion analysis of a microstrip-based negative refractive index periodic structure. *IEEE Microwave and Wireless Components Letters*, **13**(4):155-157. [doi:10.1109/LMWC.2003.811042]

Gupta, K.C., Garg, R., Bahl, I., Bhartia, P., 1996. Microstrip Lines and Slotlines. 2nd Ed., Artech House, Boston.

Ishimaru, A., Lee, S.W., Kuga, Y., Jandhyala, V., 2003. Generalized constitutive relations for metamaterials based on the Quasi-static Lorentz Theory. *IEEE Trans. Antennas Propagation*, **51**(10):2550-2557. [doi:10.1109/TAP.2003.817565]

Kong, J.A., 2002. Theorems of bianisotropic media. *Proceedings of the IEEE*, **60**(9):1036-1046.

Li, L.W., Zhang, H.X., Chen, Z.N., 2003. Representation of Constitutive Relation Tensors of Metamaterials: An Approximation for FFB Media. Proc. 2003 Progress in Electromagnetics Research (PIERS'03), Waikiki Sheraton, Hawaii, USA, p.617.

Moss, C.D., Grzegorczyk, T.M., Zhang, Y., Kong, J.A., 2002. Numerical studies of left handed metamaterials. *Progress in Electromagnetics Research*, **35**:315-334.

Oliner, A.A., 2003. A planar negative-refractive-index medium without resonant elements. *Microwave Symposium Digest, 2003 IEEE MTT-S International*, **1**:191-194. [doi:10.1109/MWSYM.2003.1210913]

Pendry, J.B., 2000. Negative refraction makes a perfect lens. *Phys. Rev. Lett.*, **85**(18):3966-3969. [doi:10.1103/PhysRevLett.85.3966]

Pendry, J.B., Holden, A.J., Stewart, W.J., Youngs, I., 1996. Extremely low frequency plasmons in metallic Meso structures. *Phys. Rev. Lett.*, **76**(25):4773-4776. [doi:10.1103/PhysRevLett.76.4773]

Pendry, J.B., Holden, A.J., Robbins, D.J., Stewart, W.J., 1999. Magnetism from conductors and enhanced nonlinear phenomena. *IEEE Trans. Microwave Theory Tech.*, **47**(11):2075-2084. [doi:10.1109/22.798002]

Sanada, A., Caloz, C., Itoh, T., 2004. Characteristics of the composite right/left-handed transmission lines. *IEEE Microwave and Wireless Components Letters*, **14**(2):68-70. [doi:10.1109/LMWC.2003.822563]

Shelby, R.A., Smith, D.R., Nemat-Nasser, S.C., Schultz, S., 2001. Microwave transmission through a two-dimensional, isotropic, left-handed metamaterial. *Applied Physics Letters*, **78**(4):489-491. [doi:10.1063/1.1343489]

Smith, D.R., Schurig, D., 2003. Electromagnetic wave propagation in media with indefinite permittivity and permeability tensors. *Physical Review Letters*, **90**(7):077405. [doi:10.1103/PhysRevLett.90.077405]

Smith, D.R., Padilla, W.J., Vier, D.C., Nemat-Nasser, S.C., Schultz, S., 2000. Composite medium with simultaneously negative permeability and permittivity. *Physical Review Letters*, **84**(18):4184-4187. [doi:10.1103/PhysRevLett.84.4184]

Song, J.M., Chew, W.C., 1995. Moment method solutions using parametric geometry. *Journal of Electromagnetic Waves and Applications*, **9**(1/2):71-83.

Veselago, V.G., 1968. The electrodynamics of substances with simultaneously negative values of ε and μ. *Soviet Physics Uspekhi*, **10**(4):509-514. [doi:10.1070/PU1968v010n04ABEH003699]

Weiland, T., Schuhmann, R., Greegor, R.B., Parazzoli, C.G., Vetter, A.M., Smith, D.R., Vier, D.C., Schultz, S., 2001. Ab initio numerical simulation of left-handed metamaterials: comparison of calculations and experiments. *Journal of Applied Physics*, **90**(10):5419-5424. [doi:10.1063/1.1410881]

Xu, W., Li, L.W., Wu, Q., 2004a. Design of Left-handed Materials with Broad Bandwidth and Low Loss Using Double Resonant Frequency Structure. 2004 IEEE AP-S International Symposium, Monterey, CA.

Xu, W., Yao, H.Y., Li, L.W., 2004b. Analysis of a novel metamaterial using TLM. *2004 International Symposium on Antennas and Propagation*, **2C3**:453-456.

Xu, W., Li, L.W., Yao, H.Y., Yeo, T.S., Wu, Q., 2005a. Extraction of constitutive relation tensor parameters of SRR structures using transmission line theory. *Journal of Electromagnetic Waves and Applications* (in press).

Xu, W., Li, L.W., Yao, H.Y., Yeo, T.S., Wu, Q., 2005b. Left-handed material effects on waves modes and resonant frequencies: filled waveguide structures and substrate-loaded patch antennas. *Journal of Electromagnetic Waves and Applications* (in press).

Yao, H.Y., Li, L.W., Wu, Q., Kong, J.A., 2004. Macroscopic Performance Analysis of Metamaterials Synthesized from Microscopic 2-D Isotropic Cross Split-Ring Resonator Array. EMW Publishing, Cambridge, Boston, **51**:197-217.

Yao, H.Y., Xu, W., Li, L.W., Wu, Q., Yeo, T.S., 2005. Propagation property analysis of metamaterial constructed by conductive SRRs and wires using the MGS-based algorithm. *IEEE Trans. Microwave Theory Tech.*, **53**(4):1469-1476. [doi:10.1109/TMTT.2005.845210]

Ziolkowski, R.W., 2003. Design, fabrication, and testing of double negative metamaterials. *IEEE Trans. Antennas Propagation*, **51**(7):1516-1529. [doi:10.1109/TAP.2003.813622]